# A conjugate heat transfer model for unconstrained melting of macroencapsulated phase change materials subjected to external convection

Hummel, Daniel; Beer, Stefan; Hornung, Andreas

[Link to publication on Research at Birmingham portal](Link to publication on Research at Birmingham portal)

# 1 Introduction

With an increasing desire for energy efficiency, latent heat thermal energy storage (LHTES) has gained increasing attention in recent years. In contrast to sensible thermal energy storage, the latent heat of fusion of a phase change material (PCM) is exploited in LHTES. Packed bed designs, involving spherical macrocapsules filled with PCM, are popular due to a relatively simple manufacturing and advantageous heat transfer properties. In these designs, the energy input and output is achieved by flow of a heat transfer fluid (HTF) around the capsules. For charging, the temperature of the HTF is higher than the melting temperature of the PCM. For discharging, the temperature of the HTF is lower than the melting temperature of the PCM. To understand and predict the underlying phenomena and to provide means for the design and dimensioning of LHTES applications, melting and solidification processes of macroencapsulated PCM are studied extensively, both experimentally and numerically.

Mathematical descriptions for melting and solidification problems can be divided into two basic approaches: Variable and fixed grid methods. In contrast to variable grid methods, fixed grid methods are characterized by not tracking the solid-liquid interface explicitly—it appears a posteriori as a feature of the solution and is expressed by a liquid or solid volume fraction field. The popular enthalpy method formulates the sets of governing equations for both phases and the condition for the progression of the solid-liquid interface in one set of equations that applies to the whole computational domain. According to [1], the use of enthalpy in the heat equation was first proposed by Eyres et al. [2] in 1946. In a series of works, the enthalpy method was refined and expanded to melting and solidification problems that involve natural convection driven flow in the melt ([3] provides an overview). As the enthalpy method provides only one velocity field for both phases, the consideration of melt flow requires dedicated treatment of the solid and liquid velocity. This is commonly accomplished by assigning a large viscosity to the solid [4], overwriting velocity values in the solid by zero [5] or by addition of a source term in the momentum equation that suppresses momentum transport in the solid [6]. The latter is commonly realized by a porosity function source term. The enthalpy-porosity method is implemented in many commercial CFD packages and has been widely used for the investigation of melting and solidification of macroencapsulated phase change materials.

Melting in macrocapsules can be divided into two phenomena: Constrained melting and unconstrained melting, also referred to as unfixed melting. In constrained melting, the motion of the remaining solid is hindered by design of the capsule or additional elements therein, such as slabs piercing the solid. In unconstrained melting, the solid PCM is not hindered from moving in the liquid PCM. The direction and intensity of this motion depends on gravity, the material properties of the PCM (in particular on the density difference between solid and liquid state) and on the thermal boundary conditions at the capsule wall. For instance, common paraffin based PCM have a positive solid to liq-

1

uid density ratio. In the case of uniform heating of the capsule, a downward motion of the solid results, leaving a thin fluid layer, or melt gap, between the bottom capsule wall and solid PCM. This phenomenon is referred to as close-contact melting. It has been reported that the melting process of paraffin wax in a spherical enclosure immersed in a water bath takes place 30% faster for unconstrained melting compared to constrained melting for the investigated parameters [7, 8]. Furthermore, as it spares any additional structures inside the capsule, unconstrained melting is considered to be the most relevant process for LHTES applications from a design and economical perspective.

However, by nature of the enthalpy-porosity method, the transition region between liquid and solid, referred to as the mushy zone, is modeled by a porosity source term that assumes the flow to behave similar like flow through a porous medium. Typically, a Carman-Kozeny approach is utilized, where porosity is replaced by the liquid volume fraction. As the liquid fraction decreases in the transition to solid, transport of momentum is increasingly suppressed and velocity in the solid is thereby set to zero. By choice of the value of the large coefficient in the Carman-Kozeny approach, also called the mushy zone constant, the intensity of suppressing momentum transport in the mushy zone and solid region is controlled. The higher the value of the mushy zone constant, the higher the suppression of momentum in the mushy zone and in the solid. Thus, the enthalpy-porosity method is intrinsically limited to the simulation of constrained melting.

In order to simulate unconstrained melting with the enthalpy method, various approaches have been reported. Most commonly, the mushy zone constant is lowered to a value that does not fully suppress velocity in the solid (e.g. [9, 10, 11]). However, this approach is problematic, as physically speaking, the solid region is not a porous medium and therefore the porosity function is not valid in the solid. By variation of the mushy zone constant, the intensity of momentum suppression in the solid cannot be varied without altering the flow resistance in the mushy zone. The solutions show a strong dependence on the value of the mushy zone constant, which is problem-specific, depends on multiple physical and numerical factors and cannot be reliably determined a priori. Therefore, different approaches for the extension of the enthalpy method to unconstrained melting problems have been proposed.

Asako et al. [12] implemented an enthalpy-viscosity method for the simulation of unconstrained, isothermal melting in a two-dimensional rectangular domain with one degree of freedom of the solid body. Inertia, gravity, pressure, and shear forces on the solid are computed in each iteration. The resultant force is assumed to be a nonlinear function of the solid velocity. By assuming a zero resultant force, the solid velocity can be computed by finding the root of the nonlinear function via Newton-Raphson method. The solid velocity is corrected iteratively inside the solution loop for enthalpy, velocity and pressure.

Rösler [13] adopted and expanded the approach of [12] to the enthalpy-

porosity method. By modification of the porosity source term similar to those found in mixture models that consider the velocity of floating dendrites in binary solid-liquid phase change problems (e.g. [14]), a prescribed solid velocity is incorporated. The solid velocity is obtained from a force balance on solid cell faces. Furthermore, by neglecting inertia forces, reformulation of the Newton-Raphson method to include force and velocity from two previous time steps was made possible, allowing for explicit and thus only one computation of the solid velocity per time step. This leads to reduction of computational effort. However, oscillations and difficulty of handling larger temperature gradients were reported [15].

Gudibande et al. [16] proposed an immersed boundary enthalpy method for the simulation of unconstrained, isothermal melting. Based on the liquid fraction field obtained by the enthalpy method, a continuous solid-liquid interface is reconstructed. At the interface, the control volumes are split into solid and liquid control volumes and a no-slip boundary condition is imposed on the interface. After solution of mass, momentum and energy equations, an integral momentum balance on the solid is solved. Taking into account the interface movement due to melting and solid motion, a remeshing step is carried out and the procedure is repeated.

Kozak et al. [17] proposed a forcing-function approach for unconstrained, isothermal melting in two dimensions with one degree of freedom of the solid body. The solid body motion is calculated based on a force balance considering weight, viscous and pressure forces on the solid. The solid body motion is accounted for by shifting solid cells according to the prescribed solid velocity. Energy conservation is imposed by decreasing, respectively increasing latent heat in cells affected by the solid motion.

Faden et al. [15] proposed an advancement of the enthalpy-porosity method by [13] with implicit incorporation of the equilibrium solid body velocity computation. They reported considerable stability and convergence improvements.

With regards to experimental investigations, in particular such that serve as validation cases for numerical methods, paraffin based PCM are commonly investigated. Paraffin based PCM are transparent in liquid state and opaque in solid state, which allows optical tracking of the phase front progression. In order to exploit this property in experiments, the PCM is filled in transparent (e.g. glass or acrylic) capsules and the heat for melting is introduced by immersing the capsule in heated water baths ([7, 8, 9, 18, 19, 20]). In the experiments, a uniform temperature in the water bath is intended. This is realized by monitoring the water bath temperature and, based on the temperature measurements, controlling the water bath temperature by an electric heater and a stirrer (e.g. [9]) or by introducing water with controlled temperature and flow rate into the test section (e.g. [20]).

Despite the measures taken to obtain a uniform bath temperature, a natural convection dominated mixed convection flow around the immersed object and a thermal boundary layer in the vicinity of the immersed object is to be expected. Judging by the experimental data available in the literature, there is little infor-

3

mation on the temporal and spatial flow and temperature field progression of the HTF and the resulting wall temperature distribution of the PCM macrocapsules. Therefore, for the simulation of the described scenarios, it is common practice to assume a constant and uniform capsule wall temperature that equals the bulk water bath temperature (e.g. [7, 9, 11, 20]). This leaves a source for uncertainty when validating numerical methods with the mentioned experiments. The uncertainty aggravates in particular if the approach of small mushy zone constants for the simulation of unconstrained melting with the enthalpy-porosity method is chosen. Therefore, for the validation of numerical methods for unconstrained melting and for a step towards a more precise simulation and thus design and dimensioning of LHTES applications, it is of great interest to consider flow and heat transport in the HTF and heat conduction in the capsule wall.

This work provides a description of both solid body motion and boundary conditions of unconstrained melting in macroencapsulated PCM subjected to external convection. Based on this description, the scenario of a spherically encapsulated PCM immersed in an initially stagnant water bath is investigated. The validity of the assumption of constant and uniform capsule wall temperatures that equal the bulk water bath temperature is evaluated.

## 2   Mathematical Model

The thermal interaction of the unconstrained melting process, conduction through the capsule wall and the flow and heat transport in the HTF is modeled. The CHT model consists of a fluid model for the heat transfer fluid region around the capsule, a solid model for the heat conduction in the capsule wall region and a solid-liquid phase change model for the region inside the capsule.

Transient heat conduction in the capsule wall is described by

$$\frac{\partial(\rho_c h_c)}{\partial t} - \text{div}(\alpha_c \rho_c \text{ grad } h_c) = 0, \tag{1}$$

where $\rho$ is density, $h$ is sensible enthalpy and $\alpha$ is thermal diffusivity. Index c denotes that the quantities are associated with the capsule wall. The flow and heat transport in the HTF is described by mass, momentum and energy conservation equations

$$\frac{\partial \rho_f}{\partial t} + \text{div}(\rho_f \vec{U}_f) = 0 \tag{2}$$

$$\frac{\partial(\rho_f \vec{U}_f)}{\partial t} + \text{grad}(\rho_f \vec{U}_f)\vec{U}_f = -\text{grad}(p_f) + \text{div}(\underline{\tau_f}) \tag{3}$$

$$\frac{\partial(\rho_f h_f)}{\partial t} + \text{div}(\rho_f \vec{U}_f h_f) + \frac{\partial(\rho_f K_f)}{\partial t} + \text{div}(\rho_f \vec{U}_f K_f) + \frac{\partial p_f}{\partial t} = \text{div}(\alpha_f \rho_f \text{ grad } h_f) + \rho_f \vec{g} \vec{U}_f, \tag{4}$$

4

where $\vec{U}$ is velocity, $K = |\vec{U}|^2/2$ is kinetic energy and $p$ is static pressure minus hydrostatic contribution $\rho \vec{g} \vec{x}$, where $\vec{g}$ and $\vec{x}$ denotes gravitational acceleration and position vectors, respectively. The viscous stress tensor is $\underline{\tau}$ and index f indicates that the quantities are associated with the HTF. The governing equations for flow and heat transport in the PCM

$$\frac{\partial \rho}{\partial t} + \mathrm{div}(\rho \vec{U}) = 0 \tag{5}$$

$$\frac{\partial(\rho \vec{U})}{\partial t} + \mathrm{grad}(\rho \vec{U})\vec{U} = -\mathrm{grad}(p) + \mathrm{div}(\underline{\tau}) + \vec{A} + \vec{B} \tag{6}$$

$$\frac{\partial(\rho h)}{\partial t} + \mathrm{div}(\rho \vec{U} h) = \mathrm{div}(\alpha \rho\ \mathrm{grad}\ h) + S \tag{7}$$

additionally include source terms $\vec{A}$, $\vec{B}$ and $S$ that arise from the enthalpy-porosity method.

**Enthalpy-porosity method**   The solid-liquid interface is not tracked explicitly. Instead, a variable for the liquid volume fraction $\alpha_{\mathrm{liq}}$ is defined and related to temperature $T$ by [21]

$$\alpha_{\mathrm{liq}} = \begin{cases} 0 & T < T_{\mathrm{melt}} \\ 1 & T > T_{\mathrm{melt}} \end{cases} \tag{8}$$

for isothermal phase change with a melting temperature $T_{\mathrm{melt}}$ and

$$\alpha_{\mathrm{liq}} = \begin{cases} 0 & T < T_{\mathrm{sol}} \\ \frac{T - T_{\mathrm{sol}}}{T_{\mathrm{liq}} - T_{\mathrm{sol}}} & T_{\mathrm{sol}} \leq T \leq T_{\mathrm{liq}} \\ 1 & T > T_{\mathrm{liq}} \end{cases} \tag{9}$$

for a binary mixture, where indices sol and liq denote the solidus and liquidus temperature. To account for the latent heat contribution in the energy equation, a source-based approach is adopted. The latent heat source term [21]

$$S = \mathrm{div}(\vec{U} \alpha_{\mathrm{liq}})\ L - \frac{\partial(\rho \alpha_{\mathrm{liq}})}{\partial t}\ L \tag{10}$$

with $L$ denoting the latent heat of fusion, is derived from the absolute enthalpy equation by expressing the absolute enthalpy as sum of sensible and latent heat [22]. In the momentum equation, a source term for the velocity treatment of the solid region is added. Instead of the common form of the Carman-Kozeny porosity source term

$$\vec{A}' = \frac{C\,(1 - \alpha_{\mathrm{liq}})^2}{\alpha_{\mathrm{liq}}^3 + q}\ \vec{U}, \tag{11}$$

the modified form [14] to incorporate a prescribed velocity in the solid

$$\vec{A} = \frac{C\left(1 - \alpha_{\text{liq}}\right)^2}{\alpha_{\text{liq}}^3 + q}(\vec{U} - \vec{U}_{\text{s}}), \tag{12}$$

is utilized. The large Carman-Kozeny, or mushy zone constant $C$, controls the flow resistance through the transition region between solid and liquid PCM and $q$ is a small constant to avoid division by zero. Index s, here describing the velocity of the solid PCM $\vec{U}_{\text{s}}$, indicates that quantities are associated with the PCM in its solid state. The modification results in the velocity field taking the values of $\vec{U}_{\text{s}}$ as $\alpha_{\text{liq}}$ tends to zero rather than setting the solid velocity to zero as achieved by Equation 11 with sufficiently large values assigned to $C$. Natural convection in the melt is taken into account by a Boussinesq approximation source term

$$\vec{B} = -\alpha_{\text{liq}}\rho_{\text{ref}}\beta\vec{g}\left(T - T_{\text{ref}}\right), \tag{13}$$

where $\beta$ is the volumetric thermal expansion coefficient and index ref denotes reference quantities. The solid PCM is modeled as a rigid body moving in the surrounding liquid PCM with three translational degrees of freedom. Rotation of the solid body is neglected in this work. The motion of the solid PCM is determined from the resultant force

$$\vec{F}_{\text{res}} = \int_{V_{\text{s}}} \rho_{\text{s}}\vec{g}\ dV_{\text{s}} + \int_{A_{\text{s}}} (p + \rho\vec{g}\vec{x})\ d\vec{A}_{\text{s}} + \int_{A_{\text{s}}} \underline{\tau} \cdot d\vec{A}_{\text{s}} \tag{14}$$

as the sum of weight, pressure and viscous forces. The volume and surface area is denoted by $V$ and $A$, respectively. As per Newton's second law of motion, the temporal derivative of the solid body velocity is given by $d\vec{U}_{\text{s}}/dt = \vec{F}_{\text{res}}/m_{\text{s}}$, where mass is denoted by $m$.

# 3 Numerical Solution

## 3.1 General solution procedure

The mathematical model was implemented in the open-source C++ library OpenFOAM® [23] (version 4.0) and was based on the original solver chtMultiRegionFoam. The solvers for the PCM, capsule wall and HTF regions are executed in a segregated, sequential manner and coupled via mixed thermal boundary conditions. The equations of each solver are discretized using the finite volume method (FVM). The pressure-velocity coupling in the PCM and HTF regions is solved in a segregated manner by the PISO algorithm [24], using a pressure correction equation obtained from the mass and momentum equations

$$\text{div}\left(\rho\mathcal{A}^{-1}\ \text{grad}\ p\right) = \frac{\partial\rho}{\partial t} + \text{div}\left(\rho\mathcal{A}^{-1}\mathcal{H} - \rho\mathcal{A}^{-1}\ \text{grad}(\rho)\ \vec{g}\vec{x}\right), \tag{15}$$

where $\mathcal{A}$ is a matrix containing the diagonal elements of the momentum equation coefficient matrix, while matrix $\mathcal{H}$ contains the off-diagonal elements.

6

## 3.2 Numerical Settings

All spatial terms were discretized by second-order schemes (linear upwind for divergence terms, central difference for gradient and Laplacian terms) while temporal terms were discretized by the first-order accurate implicit Euler method. Symmetric matrices were solved by a geometric algebraic multigrid solver with a diagonal incomplete Cholesky smoother. Asymmetric matrices were solved by a preconditioned biconjugate gradient solver with a diagonal lower-upper triangular factorization preconditioner. The mushy zone constant was set to $10^{10}$. For the reconstruction of the solid body surface, the solid-liquid interface was assumed to be located at a liquid volume fraction of 0.95. Solid velocity computation was enabled when a global liquid volume fraction of 0.02 was reached and disabled at 0.99. The solid body motion was limited to one degree of freedom (y-direction). For the reference values in the Boussinesq approximation, the liquid density and liquidus/melting temperature were chosen. The validation cases were run with adaptive time steps to meet a Courant number of 1. In order to decrease computation time for the use cases, the simulations were run with an adaptive time step to meet a maximal Courant number of 2 in the PCM. A time step sensitivity test with a maximal Courant number of 1 for both PCM and HTF yielded a maximal difference in liquid volume fraction of 0.05%.

## 3.3 Coupling of PCM, capsule wall and HTF region solvers

The solvers for each region run independently from each other but exchange values at their respective boundaries, or interfaces, for every time step. This is realized by a mixed thermal boundary condition, that requires adjacent regions to have common temperatures and heat fluxes $\vec{q}$ at the interface

$$T_1 = T_2 = T_{\mathrm{if}} \tag{16}$$

$$\vec{q}_1 = -\vec{q}_2, \tag{17}$$

where index if denotes values at the interface and indices 1 and 2 denote the regions adjacent to the interface, i.e. the HTF and capsule wall region or the capsule wall and PCM region. By expressing the heat flux based on Fourier's law of heat conduction

$$\vec{q} = k \ \mathrm{grad}(T), \tag{18}$$

where thermal conductivity is $k$, and by considering cell center values denoted by index cl and the distance between cell center and cell faces $\delta$, the interface temperature is calculated by

$$T_{\mathrm{if}} = T_{\mathrm{cl},1}\left(\frac{k_1\delta_1^{-1}}{k_1\delta_1^{-1} + k_2\delta_2^{-1}}\right) + T_{\mathrm{cl},2}\left(\frac{k_2\delta_2^{-1}}{k_1\delta_1^{-1} + k_2\delta_2^{-1}}\right). \tag{19}$$

7

## 3.4 PCM region solver

**Liquid volume fraction update**  The source-based enthalpy method [21] requires an iterative solution of the liquid volume fraction and energy equation. The liquid volume fraction is computed by

$$\alpha'_{\text{liq}} = \alpha_{\text{liq}}^{\text{o}-1} + \lambda \frac{c_p}{L} \left[ T - (2\delta T\ \alpha_{\text{liq}} + T_{\text{melt}} - \delta T) \right], \qquad (20)$$

where the value of the preceding iteration is denoted by superscript $\text{o} - 1$; $\lambda$ is a relaxation factor, $c_p$ is specific heat capacity and $\delta T$ is zero for isothermal phase change and $(T_{\text{liq}} - T_{\text{sol}})/2$ for mushy phase change. In the latter case, the melting temperature is the arithmetic mean of solidus and liquidus temperatures. To ensure boundedness, and for consideration of cells where phase change is not occurring, a correction step is carried out:

$$\alpha_{\text{liq}} = \max\left[0, \min(\alpha'_{\text{liq}}, 1)\right] \qquad (21)$$

**Solid body surface reconstruction and solid body motion**  The solid body velocity is computed for every time step. This is accomplished by the generation of a discrete surface of the solid body surface, followed by the computation of the weight, pressure and viscous forces exerted on the solid body. From the resultant forces, the solid body velocity is determined.

The surface of the solid body is reconstructed by a triangulated isosurface at a discrete liquid volume fraction value $\alpha_{\text{s}}$, above which the PCM is considered to be fully liquid (see Figures 1a and 1b). The quantities required for the computation of the forces are linearly interpolated from the cell centers of the computational mesh to the vertices of the triangulated surface, where they are averaged for each face of the triangulated surface (see Figure 1c). For the surface reconstruction and value interpolation, a regularized marching tetrahedra technique [25], which is readily available in OpenFOAM®, is utilized.

The forces exerted on the solid body are computed by

$$\vec{F}_{\text{res}} = \vec{g}\rho_{\text{s}} \sum_{\text{ce}} (\psi V)_{\text{ce}} + \sum_{\text{fc}} (\vec{n}A)_{\text{fc}} (p + \rho \vec{g}\vec{x})_{\text{fc}} + \sum_{\text{fc}} (\vec{n}A \cdot \mu \underline{\tau})_{\text{fc}}, \qquad (22)$$

where index fc denotes the faces of the reconstructed and triangulated solid body surface; $\vec{n}$ is the unit normal vector and $\mu$ is the dynamic viscosity. For the computation of the weight forces, a summation over all cells in the PCM region is carried out. To distinguish between solid and liquid cells, a nodal threshold variable $\psi$ is introduced, which is 0 if $\alpha_{\text{liq}} > \alpha_{\text{s}}$ and 1 if $\alpha_{\text{liq}} \leq \alpha_{\text{s}}$. From the resultant forces and the mass of the solid body, acceleration of the solid is computed:
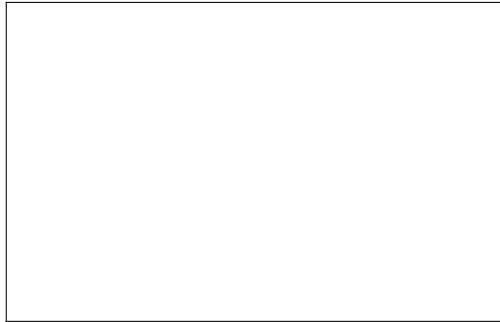
$$\vec{a}_{\text{s}} = \vec{F}_{\text{res}} \ [\rho_{\text{s}} \sum_{\text{ce}} (\psi V)_{\text{ce}}]^{-1} \qquad (23)$$

8

(a) Liquid volume fraction at x-y cross section. Detail view: Liquid volume fraction field with values and intersection of the reconstructed solid surface with $\alpha_\mathrm{s} = 0.5$.
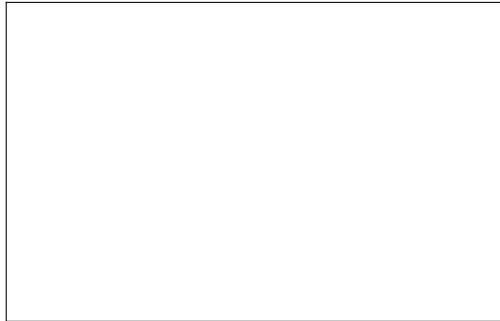


(b) Computational mesh clipped at x-y cross section and protruding reconstructed surface. Detail view: Reconstructed and triangulated surface.



(c) Volumetric pressure field clipped at x-y cross section and protruding reconstructed solid body surface with pressure field mapped to the surface. Detail view: Quantities for force computation.

Figure 1: Reconstruction of the solid body surface by example of a PCM in a spherical capsule

The solid body velocity is obtained by execution of a Newmark integration

[26] step

$$\vec{U}_{\mathrm{s}}^* = \vec{U}_{\mathrm{s}}^{\mathrm{i}-1} + \frac{\Delta t}{2} \left( \vec{a}_{\mathrm{s}} + \vec{a}_{\mathrm{s}}^{\mathrm{i}-1} \right), \tag{24}$$

incorporating solid body velocity and acceleration values of the preceding iteration i − 1 and the time step $\Delta t$. The computation of the forces and the solid velocity takes place in the inner loop. Due to the strong mutual coupling of pressure equation and the solid body velocity computation, oscillations in the pressure solution affect the solution of the solid body velocity and vice versa. In order to avoid overshoots and to ensure stability, relaxation is applied to the solid velocity

$$\vec{U}_{\mathrm{s}} = \vec{U}_{\mathrm{s}}^{\mathrm{i}-1} + \omega \left( \vec{U}_{\mathrm{s}}^* - \vec{U}_{\mathrm{s}}^{\mathrm{i}-1} \right), \tag{25}$$

where $\omega$ is a relaxation factor and where superscript $*$ denotes the unrelaxed solution of the solid velocity at the current iteration. In order to accelerate convergence, the relaxation factor is determined adaptively from the previous relaxation factor and unrelaxed and relaxed solid velocity solutions based on Aitken's $\Delta^2$-method [27, 28]

$$\omega = \omega^{\mathrm{i}-1} + (\omega^{\mathrm{i}-1} - 1) \frac{(\vec{R}^{\mathrm{i}-1} - \vec{R}) \cdot \vec{R}}{|\vec{R}^{\mathrm{i}-1} - \vec{R}|^2}, \tag{26}$$

where $\vec{R} = \vec{U}_{\mathrm{s}}^{\mathrm{i}-1} - \vec{U}_{\mathrm{s}}^*$. The solution of the solid body velocity is considered converged if the change between two subsequent iterations deceeds a user-defined tolerance

$$\max \left( \left| \frac{U_{x\mathrm{s}} - U_{x\mathrm{s}}^{\mathrm{i}-1}}{U_{x\mathrm{s}}} \right|, \left| \frac{U_{y\mathrm{s}} - U_{y\mathrm{s}}^{\mathrm{i}-1}}{U_{y\mathrm{s}}} \right|, \left| \frac{U_{z\mathrm{s}} - U_{z\mathrm{s}}^{\mathrm{i}-1}}{U_{z\mathrm{s}}} \right| \right) \leq \mathrm{tol.} \tag{27}$$

Figure 2 gives an overview of the solution algorithm of the PCM region solver. After solution of the momentum equation, the energy equation is solved and the liquid volume fraction field is updated in the outer loop until convergence is reached. After reconstruction of the solid body surface, the inner loop is entered. The solid body velocity, update of the momentum equation coefficients and solution of the pressure equation is repeated until the solid body velocity is considered converged. If the outer loop is considered converged judging by pressure and enthalpy residuals, the next time step is started.

# 4   Validation, Use Case and Discussion

## 4.1   Validation of the PCM region solver: Unconstrained Melting in Cubic Enclosure

For the validation of the PCM solver, a comparison to the works of Faden et al. [15] was carried out. They investigated unconstrained melting of an organic

Figure 2: Algorithm of the PCM region solver

PCM in a cubic enclosure with a side length of 0.04 m both experimentally and numerically. For their numerical investigation, Faden et al. utilized the method briefly described in Section 1.

### 4.1.1 Simulation Setup

The problem was assumed to be two-dimensional. Structured quadrilateral meshes with refinement at the boundaries were generated. The boundary regions occupy 1 mm from the wall and contain 15% of the cells, while the width of the innermost cell of each boundary region amounts to 35 times the width of the cell adjacent to the wall. The total cell count of the meshes is 12 769 (A1), 25 600 (A2), 51 076 (A3) and 102 400 (A4). Grid-dependence was judged by global liquid volume fraction. It was found that finer grids lead to slightly lower melting rates. Maximal differences in liquid volume fraction of 1% between A1 and A2, 0.6% between A2 and A3 and 0.4% between A3 and A4 were obtained. Mesh A2 was used for the validation.

The domain was initialized entirely filled with solid PCM at a temperature of 303.15 K. The temperatures at all walls were set to 313.15 K, while a no-slip boundary condition was applied for velocity. The pressure gradient at the walls was set to zero. The thermophysical properties (Table 1) were adopted from Faden et al. [15]. For the liquid dynamic viscosity, a linear function according to the measurements by Rösler [13] was derived.

| Property | Unit | Value/Function |
|---|---|---|
| Solidus temperature | K | 307.65 |
| Liquidus temperature | K | 309.15 |
| Latent heat of fusion | $J\,kg^{-1}$ | $220 \cdot 10^3$ |
| Density (solid) | $kg\,m^{-3}$ | 830.90 |
| Density (liquid) | $kg\,m^{-3}$ | 778.20 |
| Volumetric thermal expansion coefficient | $K^{-1}$ | $8.65 \cdot 10^{-4}$ |
| Specific heat capacity (solid) | $J\,kg^{-1}\,K^{-1}$ | 5000 |
| Specific heat capacity (liquid) | $J\,kg^{-1}\,K^{-1}$ | 2100 |
| Thermal conductivity (solid) | $W\,m^{-1}\,K^{-1}$ | 0.65 |
| Thermal conductivity (liquid) | $W\,m^{-1}\,K^{-1}$ | 0.166 |
| Dynamic viscosity ($T \leq 309.15$ K) | $Pa\,s$ | $4.4 \cdot 10^{-3}$ |
| Dynamic viscosity ($T > 309.15$ K) | $Pa\,s$ | $-9.08333 \cdot 10^{-5} \cdot T + 0.032476$ |

Table 1: Material properties used for the PCM region solver validation case

### 4.1.2 Results and Discussion

Figure 3 shows the obtained temporal progression of global liquid volume fraction in comparison to the experimental and numerical results by Faden et al. In the very beginning of the melting process, approximately up to 50 seconds, the present results differ visibly from both experimental and numerical comparison results. Up to about 300 seconds, the present results lie in between the values from the two experimental runs, while the numerical results start to exceed the experimentally obtained values from about 200 seconds on. From about 600 seconds on, the present results exceed the experimental results distinctly. Compared to the numerical results, the presently obtained values are nearly constantly and slightly lower. The melting process is completed slightly later than according to the numerical results. As shown in Figure 4, the topology of the phase boundary agrees well with the experimental photographs. The tilted solid seen in the photograph taken at 720 seconds is not reproduced by the present results. Unphysically large mushy regions and deformations of the phase boundary as seen for simulations with low mushy constant approaches cannot be established. With respect to the two experimental runs, differences of 3 and 13% in melting time are found.

Figure 5 shows the obtained solid velocity in comparison to the experimental and numerical results. Comparison is drawn to the numerical results. For a discussion on the experimental results, the reader is referred to [15]. With respect to the numerical results, the present results show an overall good agreement. The model by Faden et al. assumes force equilibrium at every time step and predicts a slightly smoother velocity progression than the present model. The mean magnitudes agree well over the entire time span. The largest differences are found between approximately 100 and 500 seconds and amount to about 5%.

Under consideration of tendentially melting rate decreasing phenomena that may occur in experiments (like gas bubbles in the melting gap, residual gas inclusions in the solid or adherence of the solid to the bottom, see [15]) and that neither gas phase nor possible three-dimensional effects were taken into account
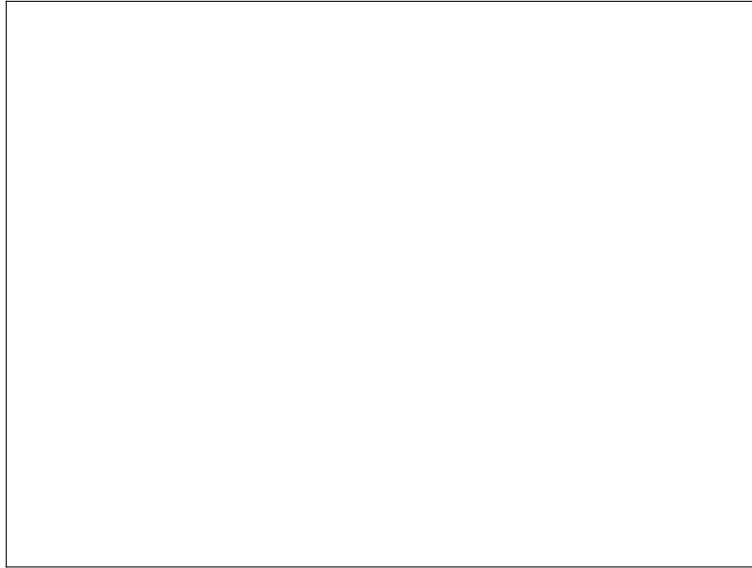
Figure 3: Global liquid volume fraction in comparison to the numerical and experimental results by [15]

in the present model, very good validation is achieved.

## 4.2 Validation of the HTF region solver: Natural Convection around a Heated Sphere immersed in a Water Bath

To analyze suitability of the HTF region solver for natural convection problems, the experiment by Amato and Tien [29] at a Rayleigh number of $1.7 \cdot 10^8$ and sphere diameter of 0.0762 m was simulated. They immersed a heated sphere with uniform wall temperature in a water bath of uniform initial temperature and measured temperature and radial velocity profiles along a line normal to the sphere surface at different angles of the sphere. For further comparison, the numerical results obtained by Yang et al. [30], who used the same case for validation purposes, were considered.

### 4.2.1 Simulation Setup

Unstructured hexahedron-dominant meshes with prismatic layers around the sphere and volumetric refinement regions above the sphere were generated. To investigate grid-dependency, three meshes with total cell counts of 188 008 (B1), 466 896 (B2) and 799 754 (B3) were considered. A tendency of lower temperatures with finer grids was observed. The maximum local difference in temperature was 3.6% between B1 and B2 and 1.5% between B2 and B3. Mesh B1 was

13

(a) This work



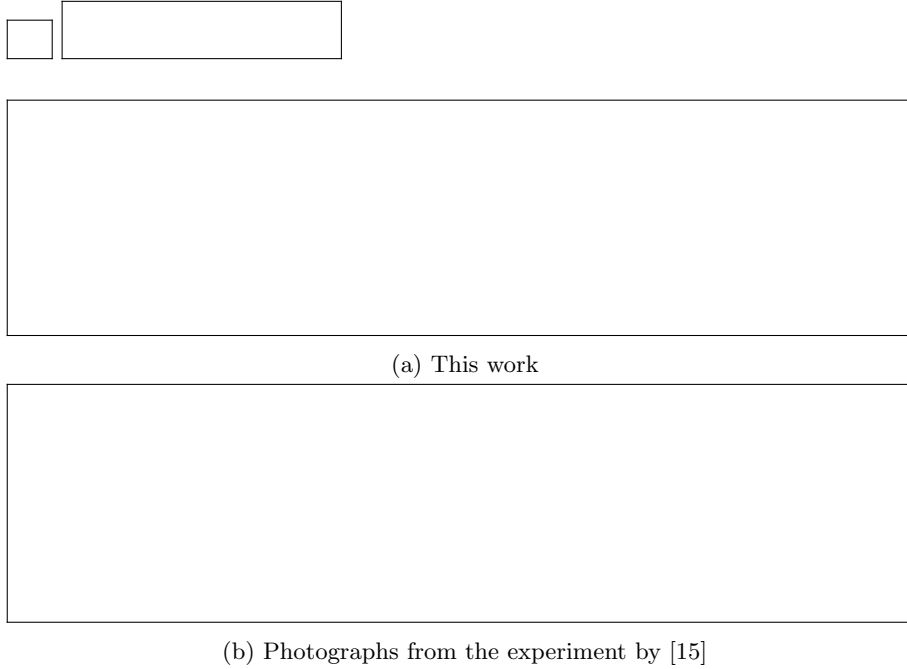(b) Photographs from the experiment by [15]

Figure 4: Phase boundaries at 120, 360, 720 and 1080 seconds (from left to right)

considered sufficient and was used for the validation computations.

385    The fluid surrounding the sphere was initialized at rest and at the lower temperature that relates to the Rayleigh number of the experiment. The uniform temperature of the sphere wall was fixed at the corresponding upper temperature. The tank walls were set to the lower temperature and a no-slip boundary condition was applied for the velocity at all walls. The pressure gradient at all

390    walls was set to zero. The temperature-dependency of the thermophysical properties of water was described by polynomials (Table 2) obtained by polynomial fitting of the data given by [31].

| Property | Unit | Function |
|---|---|---|
| Density | $\mathrm{kg\,m^{-3}}$ | $739.29 + 1.9706 \cdot T - 3.7134 \cdot 10^{-3} \cdot T^2$ |
| Specific heat capacity | $\mathrm{J\,kg^{-1}\,K^{-1}}$ | $10449 - 54.303 \cdot T - 0.15492 \cdot T^2 - 1.4517 \cdot 10^{-4} \cdot T^3$ |
| Thermal conductivity | $\mathrm{W\,m^{-1}\,K^{-1}}$ | $-2.5357 + 2.4196 \cdot 10^{-2} \cdot T - 6.1838 \cdot 10^{-5} \cdot T^2 + 5.3795 \cdot 10^{-8} \cdot T^3$ |
| Dynamic viscosity | $\mathrm{Pa\,s}$ | $0.12247 - 1.0572 \cdot 10^{-3} \cdot T + 3.0643 \cdot 10^{-6} \cdot T^2 - 2.972 \cdot 10^{-9} \cdot T^3$ |
| Volumetric thermal expansion coefficient | $\mathrm{K^{-1}}$ | $-2.8017 \cdot 10^{-2} + 2.3699 \cdot 10^{-4} \cdot T - 6.6909 \cdot 10^{-7} \cdot T^2 + 6.4495 \cdot 10^{-10} \cdot T^3$ |

Table 2: Material properties used for water
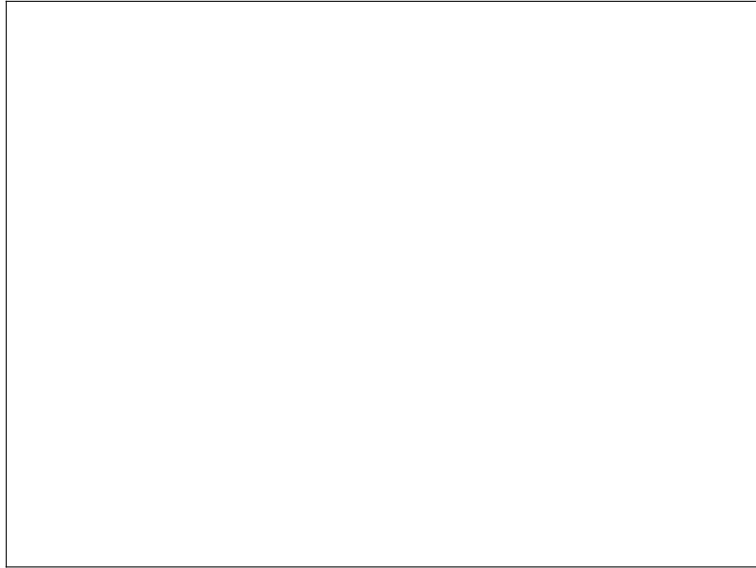
Figure 5: Solid body velocity comparison to [15]

### 4.2.2 Results and Discussion

Figure 6 shows the temperatures probed along a line of 0.005 m length normal
to sphere surface at angles of 45, 90 and 135°. For the temperatures at 90°,
very good agreement with the experiments is found, while for the remaining
angles, maximal local deviations up to roughly 20% are observed. For all probed
locations, the present computations predict lower values than the simulations
by Yang et al. Considering the uncertainty left in the experiments (e.g. the
measurements indicate a temperature lower than 1 at the wall, especially for
45 and 90°), an overall good agreement is found. The comparison to the radial
velocities (Figure 7) shows distinct differences, especially to the experimental
results. The locations of the maxima of the velocities are increasingly shifted to
positions farther away from the sphere with decreasing angles. The magnitude
of the maximal velocity is in good agreement at 90°, but is overpredicted for
45 and 135°. The qualitative progression is predicted adequately. The results
are in fair agreement with the values reported by Yang et al. for 90 and 135°,
whereby the present results show higher maximal magnitudes and the locations
of the maxima are closer to the experimental results. For 45°, velocities were
not reported by Yang et al. In their discussion, they considered errors due
to the interference of the velocity measuring probe and velocity fluctuations
in the experimental measurements to be potential sources for the deviations.
Satisfactory validation, in particular with respect to the thermal conditions
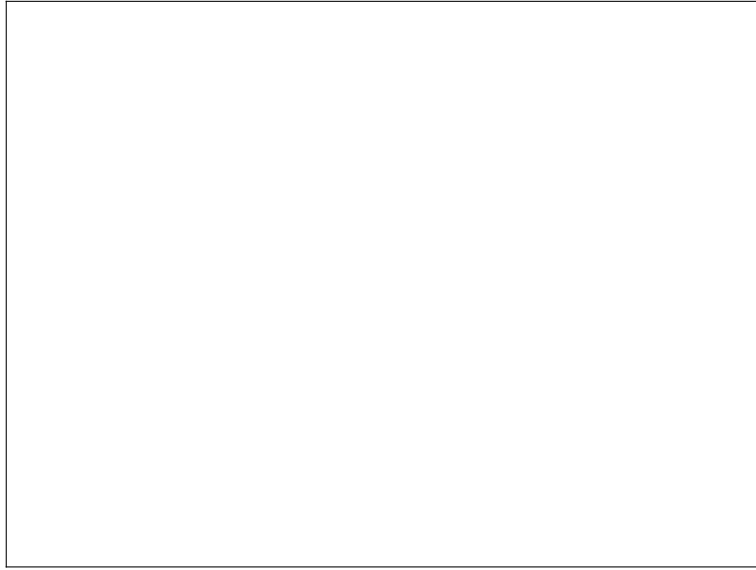around the sphere, is achieved.

15

Figure 6: Temperature along normal direction at 45, 90 and 135°, comparison to [29] and [30]
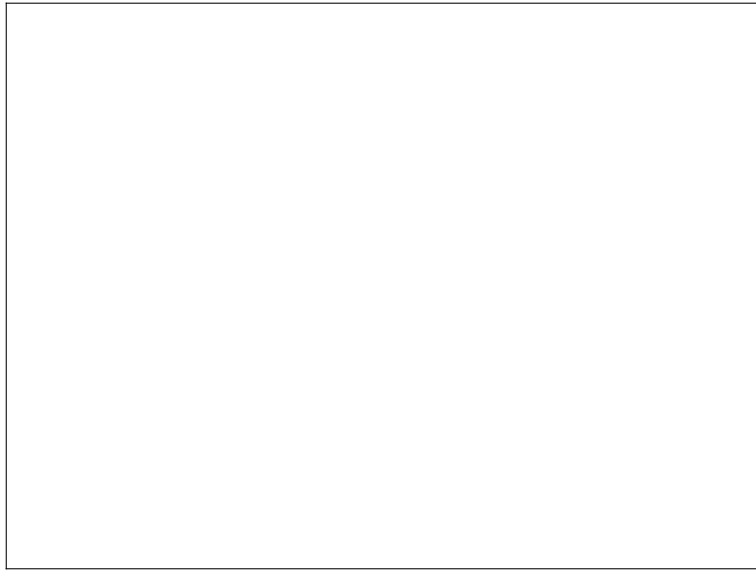


Figure 7: Radial velocity along normal direction at 45, 90 and 135°, comparison to [29] and [30]

## 4.3 Use Case: Unconstrained Melting of Spherically Encapsulated Phase Change Material Subjected to External Mixed Convection

A generic problem of unconstrained melting of a spherically encapsulated PCM immersed in a water bath was simulated to demonstrate the proposed CHT model. The problem was built along the lines of the discussed water bath experiments on unconstrained melting to gain new insights into the coupled flow and heat transfer processes of PCM, capsule wall and HTF and in particular, the resulting capsule wall temperature distribution.

Figure 8 shows the computational domain. A spherical capsule of diameter $D = 0.105$ m and wall thickness $D/70$ is located in the center of a cubic water tank with a side length of 10 $D$. The capsule was initialized completely filled with solid PCM; capsule wall and PCM were set to an initial temperature $T_0$, which lies 1 K below the melting temperature of the PCM. The HTF (water) in the tank was initialized at temperature $T_\infty$. Velocity $U_{\text{in}}$, temperature $T_\infty$ and a zero pressure gradient were defined at the inlet. At the outlet, ambient pressure was prescribed. At the adiabatic bottom, side and top walls, a no-slip condition for velocity was set.
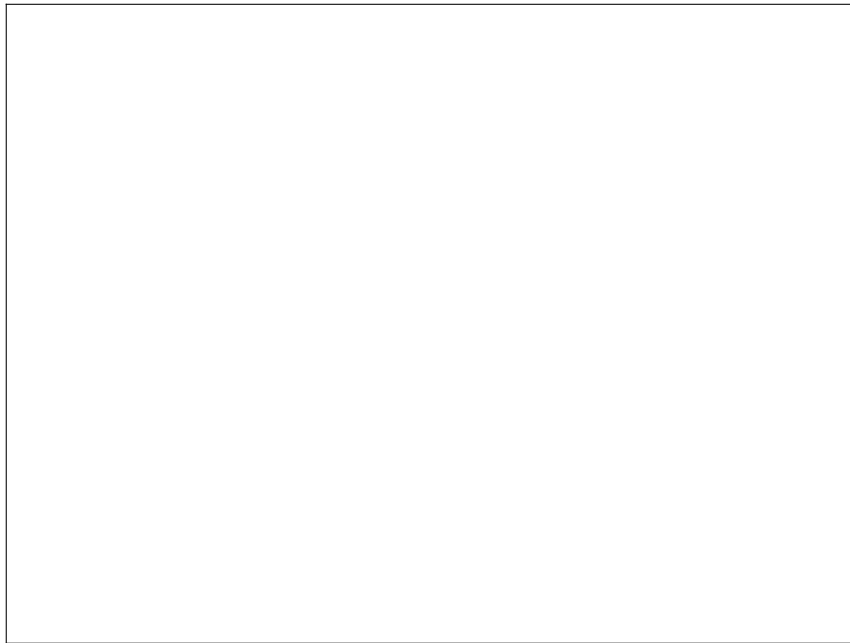


Figure 8: Computational domain for the water tank case

### 4.3.1 Simulation Setup

Unstructured hexahedron-dominant meshes were created for the HTF region. For the PCM and capsule wall regions, structured hexahedral meshes were generated. For the investigation of grid-dependence, three sets of meshes with total cell counts of 1 000 339 (C1; HTF: 222 464, PCM: 741 125, capsule wall: 36 750), 1 390 455 (C2; HTF: 318 455, PCM: 1 024 000, capsule wall: 48 000) and 2 564 607 (C3; HTF: 564 607, PCM: 1 925 000, capsule wall: 75 000) were created and analyzed. As in the melting validation case, finer meshes lead to lower melting rates. The maximal differences in global liquid fraction were 4.7% between C1 and C2 and 2.9% between C2 and C3. Considering computational effort and accuracy, C2 was chosen for all further computations.

The solid and liquid specific heat capacity of the PCM is 2000 $\mathrm{J\,kg^{-1}\,K^{-1}}$. The latent heat of fusion is $240 \cdot 10^3$ $\mathrm{J\,kg^{-1}}$. The dynamic viscosity of the PCM is $4 \cdot 10^{-3}$ $\mathrm{Pa\,s}$, the volumetric thermal expansion coefficient is $9 \cdot 10^{-4}$ $\mathrm{K^{-1}}$, the Prandtl number is 60. Melting temperature is 301 K, liquid and solid densities are 770 and 865 $\mathrm{kg\,m^{-3}}$, respectively. The thermal conductivity of the capsule is 1 $\mathrm{W\,m^{-1}\,K^{-1}}$. The temperature-dependency of the thermophysical properties of water was described by the polynomials in Table 2.

### 4.3.2 Parameter variation

The parameter study is based on the Stefan number that will be approached with temporal progression of the melting process

$$Ste_\infty = \frac{c_p \ (T_\infty - T_{\mathrm{melt}})}{L}. \tag{28}$$

Computations were carried out for $Ste_\infty$ 0.075, 0.1, 0.15, 0.2 and 0.25 by variation of the HTF initial and inlet temperature. The initial Richardson number

$$Ri_0 = \frac{g\beta_{T_\infty} D(T_\infty - T_0)}{U_{\mathrm{in}}^2}, \tag{29}$$

where the thermal volumetric expansion coefficient is obtained from the polynomial in Table 2 at initial water bath temperature, was set to $50 \cdot 10^3$ for all runs by variation of the inlet velocity.

### 4.3.3 Results and Discussion

Figure 9 shows the global liquid volume fractions obtained for $Ste_\infty$ of 0.075, 0.1, 0.15, 0.2 and 0.25. The times for completion of the melting process are 7701, 5694, 3699, 2727 and 2145 seconds, respectively.

Figure 10 shows the solid velocities obtained for $Ste_\infty$ of 0.075, 0.1, 0.15, 0.2 and 0.25. The magnitudes of the solid body velocity found are in the range of about 0.01 to 0.04 $\mathrm{mm\,s^{-1}}$. As expected, the solid body velocity increases with
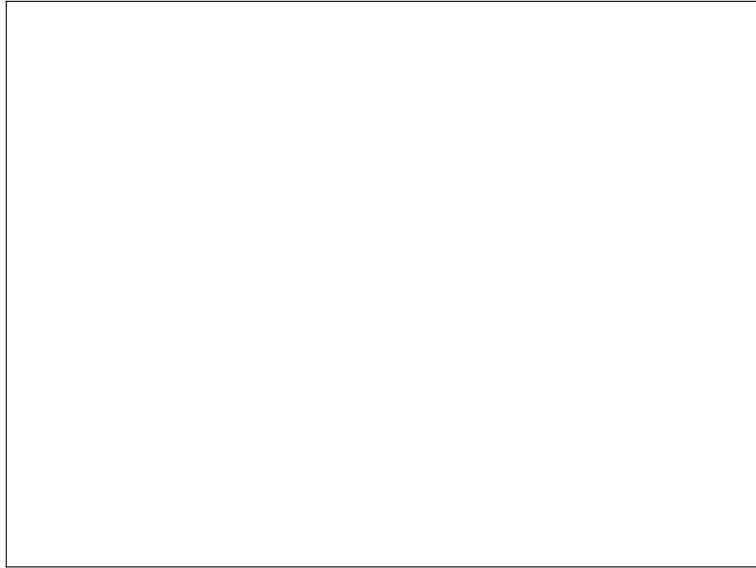
18

Figure 9: Global liquid volume fractions for $Ste_\infty$ of 0.075, 0.1, 0.15, 0.2 and 0.25

470 increasing Stefan numbers. After the very beginning of the melting process, the solid body velocity is nearly constant for each Stefan number with a slight decrease towards the end of the melting process, where fluctuations arise as the weight forces approach zero.

Figure 11 shows the heat transfer rates from the HTF to the outer capsule
475 wall obtained for $Ste_\infty$ of 0.075, 0.1, 0.15, 0.2 and 0.25. Three phases are observed: After a short period (about 250 seconds for all cases) in the beginning, where large temperature gradients between capsule and HTF are present, the heat transfer rate gradually decreases over time. This is the period where the width of the melt gap is roughly constant and a quasi steady natural convection
480 in the HTF dominates the heat transfer from the HTF to the capsule (e.g. from 500 to 4500 seconds for $Ste_\infty = 0.1$). This phase is followed by a drop in heat transfer rate as the width of the melt gap increases. Subsequently, the heat transfer rate gradually approaches zero (about 4750 to 6000 seconds for $Ste_\infty$ = 0.1).

485 Figure 12 shows the heat transfer rate from HTF to the outer capsule wall for $Ste_\infty$ of 0.1 and three regions with equal surface area. It becomes apparent that the largest amount of heat is transferred through the lower part of the sphere, while the lowest amount is transferred through the upper part.

When normalized with respect to dimensionless temperature

$$\theta = \frac{T_\infty - T}{T_\infty - T_0} \tag{30}$$
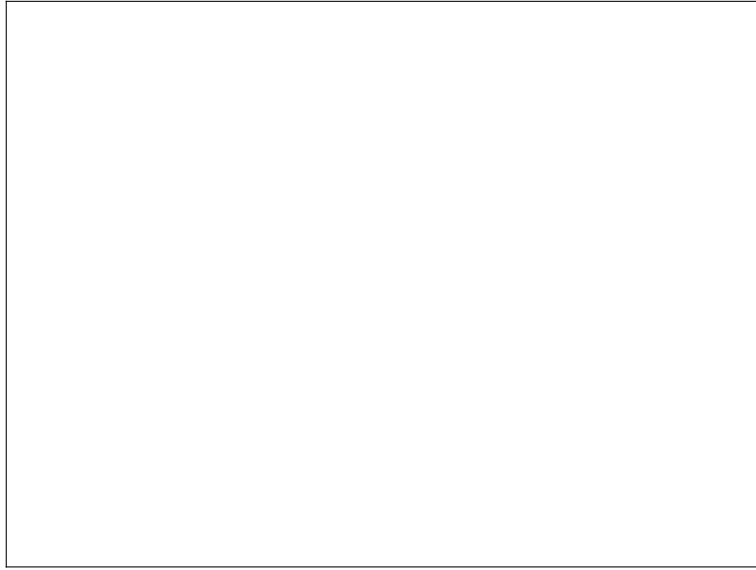
19

Figure 10: Solid velocities in y-direction for $Ste_\infty$ of 0.075, 0.1, 0.15, 0.2 and 0.25
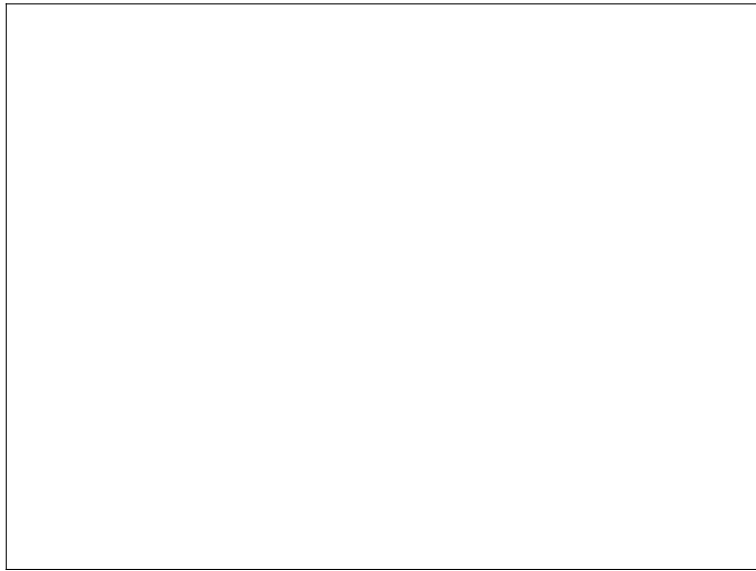


Figure 11: Heat transfer rate from HTF to the outer capsule wall for $Ste_\infty$ of 0.075, 0.1, 0.15, 0.2 and 0.25

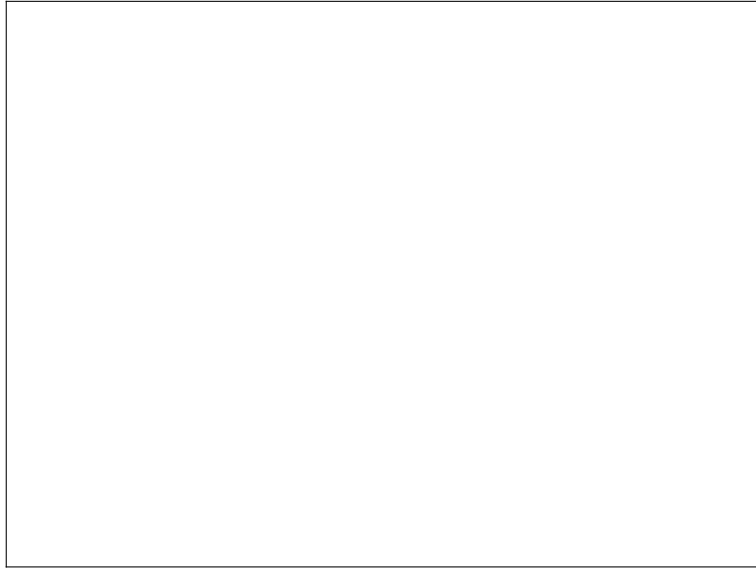490    and dimensionless time

$$\xi = t/t_{\text{melt}}, \tag{31}$$

20

Figure 12: Heat transfer rate from HTF to the outer capsule wall for $Ste_\infty$ of 0.1 and three regions with equal surface area

where $t_{\mathrm{melt}}$ is the melting completion time, the solutions obtained for the investigated range of $Ste_\infty$ are identical with slight variations due to the non-linearities in the thermophysical properties of water. Therefore, for the sake of transferability, results obtained for $Ste_\infty$ of 0.1 are shown under specification of these dimensionless numbers. Figure 13 shows the temperature profiles along a line at the x-y cross section surface for the inner and outer capsule wall at three different times $\xi = 0.1$, 0.5 and 0.9. First of all, it confirms the hypothesis of this work and the observation made with respect to the heat transfer rate through the lower, mid and upper sections of the capsule: The temperature distribution at the capsule wall is transient and highly non-uniform. At low angles (the lower region) the lowest temperatures are found. Near the top of the sphere, the capsule temperature is closer to the water bath temperature, even at early times. With progression of the melting process, the temperature distribution becomes more uniform. However, halfway through the melting progress the lowest temperature at the inner capsule wall merely amounts to 0.1, while at the outer capsule wall roughly 0.3 is reached. The temperature gradient between the inner and outer capsule wall becomes smaller with time and its minimum shifts towards lower regions as time progresses.

Figure 14 shows temperature contours in the HTF and capsule wall and the liquid volume fraction inside the capsule at the x-y cross section for $\xi = 0.005$, 0.006, 0.0075, 0.008, 0.01, 0.025, 0.05, 0.1, 0.3, 0.5, 0.7 and 0.9. After the immersion of the subcooled capsule into the water bath, high temperature gradients are present and unsteady natural convection occurs. The temperature
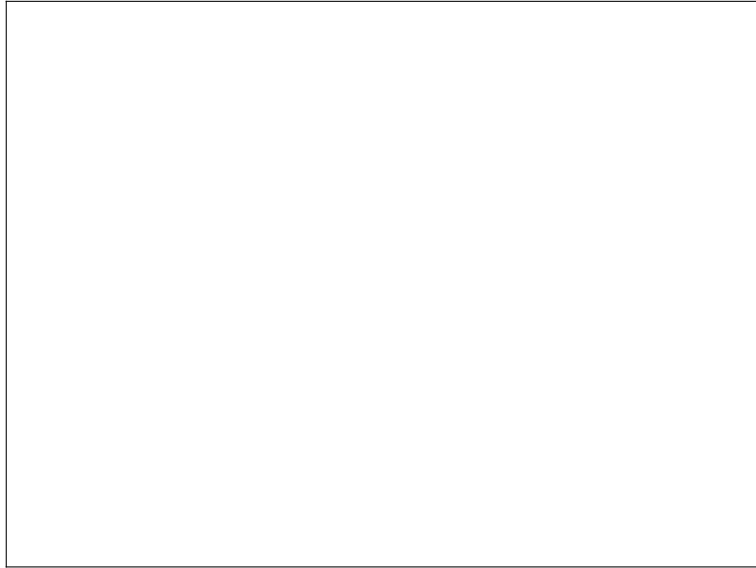
Figure 13: Temperature profiles along a line at the x-y cross section surface of the inner and outer capsule walls at three different times $\xi = 0.1$, 0.5 and 0.9

fields show a clear transient characteristic up to about a dimensionless time
of 0.025. With progression of the melting process, the temperature gradients
decrease and a quasi steady state is observed from $\xi = 0.025$ to 0.9. When
the melting process is almost completed, the non-uniformity of the capsule wall
temperature decreases and the capsule wall increasingly reaches water bath
temperature. With further decreasing temperature gradients, natural convec-
tion becomes weak enough that forced convection, even at the high Richardson
number investigated, gains minor influence (see the slight deflection in direction
of the inlet velocity at $\xi = 0.9$).

Figures 15 and 16 show the temporal progression of temperatures in the
HTF taken at different diameters around the capsule. Figure 15 shows the
temperature probes beneath the sphere, while Figure 16 shows the probes in the
remaining directions. In Figure 15, the expected tendencies become apparent:
The closer the probe is located to the sphere surface, the lower the temperature
becomes. With progression in time, the temperatures rise towards the initial
water bath temperature. Figure 16 shows that the water bath temperature in
any other direction is not affected significantly. In an experimental context,
the temperature variations in any other water bath location than beneath the
sphere are well below the detection limit of common measurement techniques.

The analyses of the results carried out up to this point clearly emphasize
that the assumption of constant and uniform capsule wall temperatures, equal to
the bulk water bath temperatures, does not hold for the investigated scenarios.
However, the question arises to which extent the assumption affects the simu-

22

Figure 14: Temperature contours in HTF and capsule wall and PCM liquid volume fraction at the x-y cross section for $\xi = 0.005$, 0.006, 0.0075, 0.008, 0.01, 0.025, 0.05, 0.1, 0.3, 0.5, 0.7 and 0.9

lation results. Therefore, computations with uniform capsule wall temperature at Stefan numbers

$$Ste = \frac{c_p \ (T_{\text{wall}} - T_{\text{melt}})}{L} \tag{32}$$

of 0.075, 0.1, 0.15, 0.2 and 0.25 were carried out under the assumption in
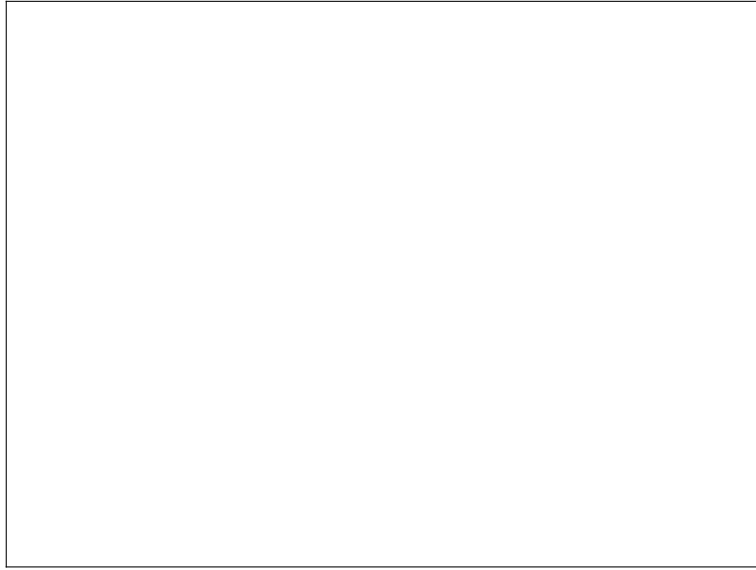
23

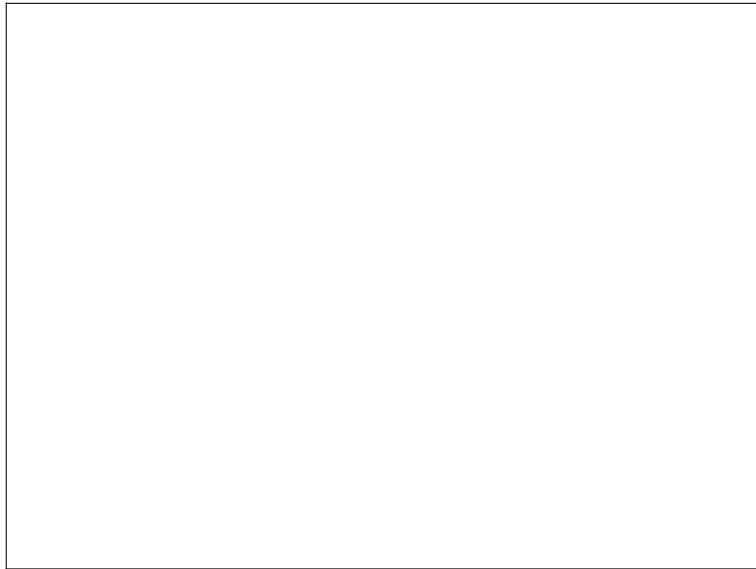Figure 15: Temperatures taken at probes in the HTF, negative y-direction



Figure 16: Temperatures taken at probes in the HTF, positive and negative x and z-directions and positive y-direction

question. For the comparison, the PCM region solver of the proposed CHT model was used without being coupled to the HTF and capsule wall solvers. Besides that, the simulation was performed applying identical boundary condi-

24

tions and by use of the identical settings and mesh.

Figure 17 compares the global liquid volume fraction curve obtained by the CHT model against the results obtained under the assumption $T_{\text{wall}} = T_\infty$ for $Ste$ or $Ste_\infty$ of 0.075, 0.15, 0.25. The expectation that the assumption leads to higher melting rates is confirmed and the influence is found to be significant. The times for completion of the melting process are 3816, 2988, 2028, 1611 and 1277 seconds for Stefan numbers of 0.075, 0.1, 0.15, 0.2 and 0.25, respectively, amounting to errors of 50.4, 45.4, 45.1, 40.9 and 40.5%.

Figure 17: Comparison of the liquid fraction curves between conjugate heat transfer model and fixed capsule wall temperatures that equal the bulk water bath temperature

# 5 Summary and Conclusions

A conjugate heat transfer model for the simulation of unconstrained melting of macroencapsulated PCM subject to external convective heat transfer was presented. In the PCM region of the CHT model, a modified form of the enthalpy-porosity method for considering solid body velocity in unconstrained melting was proposed. The modified method comprises reconstruction of the solid surface by an isosurface and solid body velocity computation via integration of the acceleration obtained from the forces exerted on the solid body. Convergence of the solid body velocity computation is accelerated by Aitken's relaxation.

After validation of the PCM and HTF region solvers, a generic case of the popular experiments of a spherically encapsulated PCM immersed in a water

bath was simulated. New insights on the progression of flow and heat transport in the HTF and capsule wall have been gained. For unconstrained melting processes where the spherical capsule is subject to external heat transfer dominated by natural convection, the temperature distribution on the capsule wall is transient and highly non-uniform. The assumption of constant and uniform wall temperatures leads to significant errors for the investigated scenarios. To provide an adequate basis for validation of numerical methods, experiments of encapsulated PCM subject to external convection necessitate detailed monitoring of the temporal and spatial progression of flow and temperature fields in the HTF and capsule wall.

# Declaration of Interest

The authors declare that they have no known competing financial interests or personal relationships that could have appeared to influence the work reported in this paper.

# References

# References

[1] J. Crank, Free and Moving Boundary Problems, Oxford University Press, 1984.

[2] N. R. Eyres, D. R. Hartree, J. Ingham, R. Jackson, R. J. Sarjant, J. B. Wagstaff, The calculation of variable heat flow in solids, Philosophical Transactions of the Royal Society A: Mathematical, Physical and Engineering Sciences 240 (813) (1946) 1–57. doi:10.1098/rsta.1946.0002.

[3] Voller, An overview of numerical methods for solving phase change problems, in: Advances in Numerical Heat Transfer, CRC Press, 1996, pp. 341–375.

[4] D. K. Gartling, Finite element analysis of convective heat transfer problems with change of phase, in: Computer Methods in Fluids, Pentech Press, 1980, pp. 257–284.

[5] K. Morgan, A numerical analysis of freezing and melting with convection, Computer Methods in Applied Mechanics and Engineering 28 (3) (1981) 275–284. doi:10.1016/0045-7825(81)90002-5.

[6] V. Voller, C. Prakash, A fixed grid numerical modelling methodology for convection-diffusion mushy region phase-change problems, International Journal of Heat and Mass Transfer 30 (8) (1987) 1709–1719. doi:10.1016/0017-9310(87)90317-6.

[7] F. Tan, Constrained and unconstrained melting inside a sphere, International Communications in Heat and Mass Transfer 35 (4) (2008) 466–475. `doi:10.1016/j.icheatmasstransfer.2007.09.008`.

[8] S. A. Khot, N. K. Sane, B. S. Gawali, Experimental investigation of phase change phenomena of paraffin wax inside a capsule, International Journal of Engineering Trends and Technology (2011) 67–71.

[9] E. Assis, L. Katsman, G. Ziskind, R. Letan, Numerical and experimental study of melting in a spherical shell, International Journal of Heat and Mass Transfer 50 (9) (2007) 1790–1804. `doi:10.1016/j.ijheatmasstransfer.2006.10.007`.

[10] F. Tan, S. Hosseinizadeh, J. Khodadadi, L. Fan, Experimental and computational study of constrained melting of phase change materials (PCM) inside a spherical capsule, International Journal of Heat and Mass Transfer 52 (15-16) (2009) 3464–3472. `doi:10.1016/j.ijheatmasstransfer.2009.02.043`.

[11] S. Hosseinizadeh, A. Rabienataj Darzi, F. Tan, J. Khodadadi, Unconstrained melting inside a sphere, International Journal of Thermal Sciences 63 (2013) 55–64. `doi:10.1016/j.ijthermalsci.2012.07.012`.

[12] Y. Asako, M. Faghri, M. Charmchi, P. A. Bahrami, Numerical solution for melting of unfixed rectangular phase-change material under low-gravity environment, Numerical Heat Transfer, Part A: Applications 25 (2) (1994) 191–208. `doi:10.1080/10407789408955944`.

[13] F. Rösler, Modellierung und Simulation der Phasenwechselvorgänge in makroverkapselten latenten thermischen Speichern, Dissertation, Universität Bayreuth (2014).

[14] W. Bennon, F. Incropera, A continuum model for momentum, heat and species transport in binary solid-liquid phase change systems—i. model formulation, International Journal of Heat and Mass Transfer 30 (10) (1987) 2161–2170. `doi:10.1016/0017-9310(87)90094-9`.

[15] M. Faden, A. König-Haagen, S. Höhlein, D. Brüggemann, An implicit algorithm for melting and settling of phase change material inside macrocapsules, International Journal of Heat and Mass Transfer 117 (2018) 757–767. `doi:10.1016/j.ijheatmasstransfer.2017.10.033`.

[16] N. Gudibande, K. Iyer, Numerical simulation of contact melting using the cell-splitting modified enthalpy method, Numerical Heat Transfer, Part B: Fundamentals 71 (1) (2017) 84–107. `doi:10.1080/10407790.2016.1244396`.

[17] Y. Kozak, G. Ziskind, Novel enthalpy method for modeling of PCM melting accompanied by sinking of the solid phase, International Journal of Heat and Mass Transfer 112 (2017) 568–586. `doi:10.1016/j.ijheatmasstransfer.2017.04.088`.

27

[18] P. A. Bahrami, T. G. Wang, Gravity and conduction driven melting in a sphere, MRS Proceedings 87 (1986) 271. `doi:10.1557/PROC-87-271`.

[19] A. Regin, S. Solanki, J. Saini, Experimental and numerical analysis of melting of PCM inside a spherical capsule, in: 9th AIAA/ASME Joint Thermophysics and Heat Transfer Conference, American Institute of Aeronautics and Astronautics, 2006, pp. 1–12. `doi:10.2514/6.2006-3618`.

[20] D. Ghosh, C. Guha, Numerical and experimental investigation of paraffin wax melting in spherical cavity, Heat and Mass Transfer 55 (5) (2019) 1427–1437. `doi:10.1007/s00231-018-2522-0`.

[21] C. R. Swaminathan, V. R. Voller, A general enthalpy method for modeling solidification processes, Metallurgical Transactions B 23 (5) (1992) 651–664. `doi:10.1007/BF02649725`.

[22] V. R. Voller, M. Cross, N. C. Markatos, An enthalpy method for convection/diffusion phase change, International Journal for Numerical Methods in Engineering 24 (1) (1987) 271–284. `doi:10.1002/nme.1620240119`.

[23] H. G. Weller, G. Tabor, H. Jasak, C. Fureby, A tensorial approach to computational continuum mechanics using object-oriented techniques, Computers in Physics 12 (6) (1998) 620. `doi:10.1063/1.168744`.

[24] R. I. Issa, Solution of the implicitly discretised fluid flow equations by operator-splitting, Journal of Computational Physics 62 (1986) 40–65. `doi:10.1016/0021-9991(86)90099-9`.

[25] G. Treece, R. Prager, A. Gee, Regularised marching tetrahedra: improved iso-surface extraction, Computers & Graphics 23 (4) (1999) 583–598. `doi:10.1016/S0097-8493(99)00076-X`.

[26] N. M. Newmark, A method of computation for structural dynamics, American Society of Civil Engineers, 1959.

[27] A. C. Aitken, XXV.—On bernoulli's numerical solution of algebraic equations, Proceedings of the Royal Society of Edinburgh 46 (1927) 289–305. `doi:10.1017/S0370164600022070`.

[28] B. M. Irons, R. C. Tuck, A version of the aitken accelerator for computer iteration, International Journal for Numerical Methods in Engineering 1 (3) (1969) 275–277. `doi:10.1002/nme.1620010306`.

[29] W. S. Amato, C. Tien, Free convection heat transfer from isothermal spheres in water, International Journal of Heat and Mass Transfer 15 (2) (1972) 327–339. `doi:10.1016/0017-9310(72)90078-6`.

[30] S. Yang, V. Raghavan, G. Gogos, Numerical study of transient laminar natural convection over an isothermal sphere, International Journal of Heat and Fluid Flow 28 (4) (2007) 821–837. `doi:10.1016/j.ijheatfluidflow.2006.08.004`.

[31] VDI e. V. (Ed.), VDI-Wärmeatlas, Springer Berlin Heidelberg, 2013. `doi:10.1007/978-3-642-19981-3`.